Available online at www.sciencedirect.com
ScienceDirect
Trans. Nonferrous Met. Soc. China 35(2025) 3561−3577
Transactions of Nonferrous Metals Society of China
www.tnmsc.cn

Composition design of high-strength and heat-resistant Al−Si−Fe alloy for powder bed fusion using laser beam

Wen-zhe GAO[1], Li ZHANG[1,2], Kai-yang LI[3], Xiao-hui YANG[4], Jin-fang ZHANG[1], Jian-hong WANG[1], Hong XU[1], Pei-kang BAI[1], Yuan-kui CAO[5], Bin LIU[5], Xiao-feng LI[1,5]

1. School of Materials Science and Engineering, North University of China, Taiyuan 030051, China;
2. Institute of Special Metal Materials and Equipment, North University of China, Taiyuan 030051, China;
3. School of Energy Power and Mechanical Engineering, North China Electric Power University, Beijing 102206, China;
4. Advanced Manufacturing and Intelligent Equipment Industrial Research Institute, Hai'an & Taiyuan University of Technology, Hai'an 226600, China;
5. State Key Laboratory of Powder Metallurgy, Central South University, Changsha 410083, China

Received 28 February 2024; accepted 21 November 2024

Abstract: A combination of casting and laser remelting was employed to develop a high-strength and heat-resistant Al−Si−Fe alloy suitable for powder bed fusion using a laser beam (PBF-LB). By clarifying the effects of the incorporated elements and their contents on the microstructure and mechanical performance of Al−Si−Fe alloys, the composition was optimized as Al−11Si−2.5Fe−2Mn−1.2Ni−0.4Cr (in wt.%). The optimized alloy was subsequently validated using PBF-LB, which exhibited favorable machinability, achieving a density of 99.8%. The room-temperature tensile strength of the PBF-LB manufactured Al−Si−Fe alloy reached (512.76±3.26) MPa, with a yield strength of (337.79±2.36) MPa and an elongation of (2.98±0.07)%. The enhanced room-temperature mechanical properties could be mainly attributed to the combined effects of fine-grain strengthening, solid solution strengthening, and precipitation strengthening. At 300 °C, the high-temperature tensile strength of the developed alloy reached (222.47±6.41) MPa, with a yield strength of (164.25±11.40) MPa and an elongation of (8.88±0.33)%, outperforming those of existing alloys documented in the literature. The improved high-temperature mechanical performance was primarily provided by the three-dimensional network comprising cellular heat-resistant $Al_{17}(FeMnNiCr)_4Si_2$ and α-Al(FeMn)Si phases.

Key words: Al−Si−Fe alloy; laser powder bed fusion; alloy composition optimization; heat-resistant phase; strengthening mechanism

1 Introduction

Known for their lightweight, high specific strength, good corrosion resistance, and easy processing characteristics, aluminum alloys have potential applications in the aerospace and automotive industries [1]. The utilization of powder bed fusion using a laser beam (PBF-LB) in the manufacturing of aluminum alloys enables the reduction of manufacturing lead time through replacing a series of production processes with a single-step process [2]. Extensive research has been conducted on the PBF-LB of Al−Si alloys, such as Al−12Si and AlSi10Mg [3]. These eutectic or hypoeutectic Al−Si alloys have been proved to be

Corresponding author: Li ZHANG, Tel: +86-13166020027, E-mail: zhli2020@nuc.edu.cn;
Xiao-feng LI, Tel: +86-13633518635, E-mail: lxf@nuc.edu.cn
https://doi.org/10.1016/S1003-6326(25)66899-3

particularly well-suited for PBF-LB printing due to their low melting point, narrow solidification temperature range, and low shrinkage rate. The room-temperature mechanical performance of the Al−Si alloy has been repeatedly reported to be better than that of the conventionally processed counterpart. The improved strength is attributed to the presence of sub-grain boundaries and inter-dendritic Si, which inhibit dislocation movement [4−8]. However, these alloys exhibit inferior high-temperature performance due to the fracture of silicon-rich grain boundaries [9].

The heat resistance of aluminum alloys can be enhanced through the introduction of alloying elements [10]. It is essential that the selected elements possess the capacity to form thermally stable phases and exhibit low diffusivity [11]. Furthermore, the mobility of grain boundaries and dislocations can be greatly reduced by forming a high volume fraction of heat-resistant phases [12]. By adding Fe and Ni elements into the cast Al−Si alloy, interconnected intermetallic compounds can be formed, thereby improving the high-temperature performance of the alloy [13]. However, the presence of coarse needle-like or plate-like β-Fe has a detrimental effect on the strength and elongation of the alloy. To mitigate the adverse effects of β-Fe, elements such as Ni, Mn, and Cr are commonly incorporated with the objective of converting the β-Fe phase to α-Fe phase. WANG et al [14] investigated the influence of Mn and Cr elements on the formation of Fe-rich intermetallic compounds in Al−Si−Cu alloys, and the results indicated that the addition of Mn and Cr reduced the size of the Fe-rich phase and changed the structure of the Fe-rich phase from β phase to α phase, eventually improving the mechanical properties of Al−Si−Cu alloy. LIN et al [15] investigated the influence of Cr on the microstructure and mechanical properties of a heat-resistant Al−12Si−3.5Cu−2Mn (wt.%) alloy. The results showed that the addition of Cr significantly altered the morphology of the Mn-rich primary phase, evolving from elongated rod-like structures to dendrites and subsequently to star-shaped particles, thereby enhancing its high-temperature strength. Numerous studies [11−14,16] have been conducted on the development of cast heat-resistant Al−Si alloys, with fewer studies on alloy produced through PBF-LB. Besides, though the shape of the heat-resistant phases can be controlled by alloying during the casting process, these phases remain substantial in size and irregular in shape.

PBF-LB exhibits a higher cooling rate compared to casting. As a result, the processing of Al−Si−Fe alloys via PBF-LB can result in the production of finer and more precise phases and microstructures, thus improving the high-temperature mechanical properties. MANCA et al [17] employed PBF-LB to produce an Al−12Si−1.4Fe−1.4Ni (wt.%) alloy. The resulting fine structure was composed of submicron Si, $Al_5Fe(Ni,Cu)$, and $Al_3(Ni,Cu)$ phases, and this alloy exhibited a compressive strength of 355 MPa at 200 °C. XIAO et al [8] used PBF-LB to manufacture an AlSi12FeMn alloy containing 0.54 wt.% Fe. The process resulted in the formation of spherical nanoscale α-Al(FeMn)Si phases, with a diameter of 10−50 nm. RAKHMONOV et al [18] used PBF-LB to manufacture an Al−3.6Mn−2.0Fe−1.8Si−0.9Zr (wt.%) alloy, resulting in the formation of sub-micron spherical α-Al(FeMn)Si phases that were distributed widely at the grain boundaries and within the grains. These phases acted as nucleating agents, facilitating the refinement of the grain structure and significantly enhancing the creep resistance of the alloy.

The heat-resistant temperature of Al−Si alloys is currently limited to approximately 250 °C [15,19], making it necessary to develop a new kind of Al−Si−Fe alloys that is not only suitable for PBF-LB but also exhibits a superior high-temperature performance. To develop this new alloy in a cost-effective and expeditious manner, a combination of casting and laser-remelting can be used. In this study, a total of nine distinct Al−Si alloy compositions were firstly designed through an orthogonal method, incorporating different contents of Fe, Mn, Ni and Cr. Subsequently, a combination of casting and laser-remelting was used to fabricate the designed alloys. The optimal Al−Si−Fe alloy composition was determined through comparing the microstructure and mechanical properties of the laser remelted zones. Ultimately, the alloy composition was validated by PBF-LB, and the high-temperature properties of the fabricated alloy and its strengthening mechanism were investigated.

2 Experimental

2.1 Material preparation

As previously stated, the enhancement of high-temperature strength in aluminum alloys necessitates the generation of an adequate number of heat-resistant phases through the combination of high contents of the fast-diffusing element, such as Si, and the slow-diffusing elements, such as Fe and Ni. Consequently, novel heat-resistant aluminum alloys were developed based on the Al−11Si series alloys. Table 1 lists the compositions of the designed alloys.

The casting process commenced with the placement of pure aluminum in a resistance furnace, which was heated at a rate of 20 °C/min. Once the pure aluminum was completely melted and the temperature reached 780 °C, the Si, Cr, and Fe powders, wrapped in aluminum foil, were introduced into the melt. Following this, the Al−10Ni and Al−10Mn master alloys were added. The melt was then stirred thoroughly to ensure complete dissolution of all alloying elements. Subsequently, it was cooled to 745 °C and degassed using C_2Cl_6. After a period of 10−15 min, the melt was cooled to 690 °C for casting in a metal-type mould.

Prior to the laser-remelting process, the samples were cut into the desired shape (10 mm × 10 mm × 10 mm) by a wire electrical discharge machining, polished successively using $600^{\#}$−$1500^{\#}$ sandpaper, and then darkened with a marker to reduce the laser reflectivity. Subsequently, an IPG YLR−2000 fiber laser was employed for single-layer single-pass laser remelting on the as-cast alloy surfaces. The laser parameters employed during the remelting process were set as follows: a laser power of 1000 W, a scanning speed of 20 mm/s, a spot diameter of 1.5 mm, and an argon gas atmosphere.

Once the optimal chemical composition of the Al−Si−Fe alloy was determined, the corresponding powder was prepared and printed using PBF-LB for the purpose of validation. The powder was prepared by vacuum air atomization, and the actual chemical composition determined by ICP-AES was Al−10.88Si−2.65Fe−1.86Mn−1.13Ni−0.38Cr (in wt.%). As shown in Figs. 1(a, b), the morphology of the prepared powder is nearly spherical, and the particle size follows a normal distribution, with D_{10}, D_{50}, and D_{90} being 22.08, 36.31, and 58.52 μm, respectively.

The equipment used for PBF-LB was the EP-M150 machine (E-Plus−3D, Beijing, China). Before printing, the powder was dried in a vacuum oven at 110 °C for 2−4 h. The optimized PBF-LB process parameters were as follows: a laser power of 310 W, a scanning speed of 1400 mm/s, a powder layer thickness of 30 μm, and scanning strategy involving a 67° rotation between the layers, with a hatch distance of 90 μm, and an argon gas atmosphere. An AA6083 alloy was utilized as the substrate, which was maintained at 140 °C throughout the fabrication process.

2.2 Characterization

Prior to the microstructural characterization, a standard metallographic technique was implemented for the as-cast and laser-remelted samples, including mechanical grinding with successively finer-grained SiC papers and final polishing with a MgO suspension. This was followed by etching with Keller's reagent for 6−8 s.

Table 1 Compositions of designed alloys (wt.%)

Alloy	Composition	A(Fe)	B(Mn)	C(Ni)	D(Cr)	E(Si)	F(Al)
1#	Al−11Si−2.5Fe−1.5Mn−0.4Ni−0.2Cr	2.5	1.5	0.4	0.2	11	Bal.
2#	Al−11Si−2.5Fe−2.0Mn−0.8Ni−0.4Cr	2.5	2.0	0.8	0.4	11	Bal.
3#	Al−11Si−2.5Fe−2.5Mn−1.2Ni−0.6Cr	2.5	2.5	1.2	0.6	11	Bal.
4#	Al−11Si−3.0Fe−1.5Mn−0.8Ni−0.6Cr	3.0	1.5	0.8	0.6	11	Bal.
5#	Al−11Si−3.0Fe−2.0Mn−1.2Ni−0.2Cr	3.0	2.0	1.2	0.2	11	Bal.
6#	Al−11Si−3.0Fe−2.5Mn−0.4Ni−0.4Cr	3.0	2.5	0.4	0.4	11	Bal.
7#	Al−11Si−3.5Fe−1.5Mn−1.2Ni−0.4Cr	3.5	1.5	1.2	0.4	11	Bal.
8#	Al−11Si−3.5Fe−2.0Mn−0.4Ni−0.6Cr	3.5	2.0	0.4	0.6	11	Bal.
9#	Al−11Si−3.5Fe−2.5Mn−0.8Ni−0.2Cr	3.5	2.5	0.8	0.2	11	Bal.

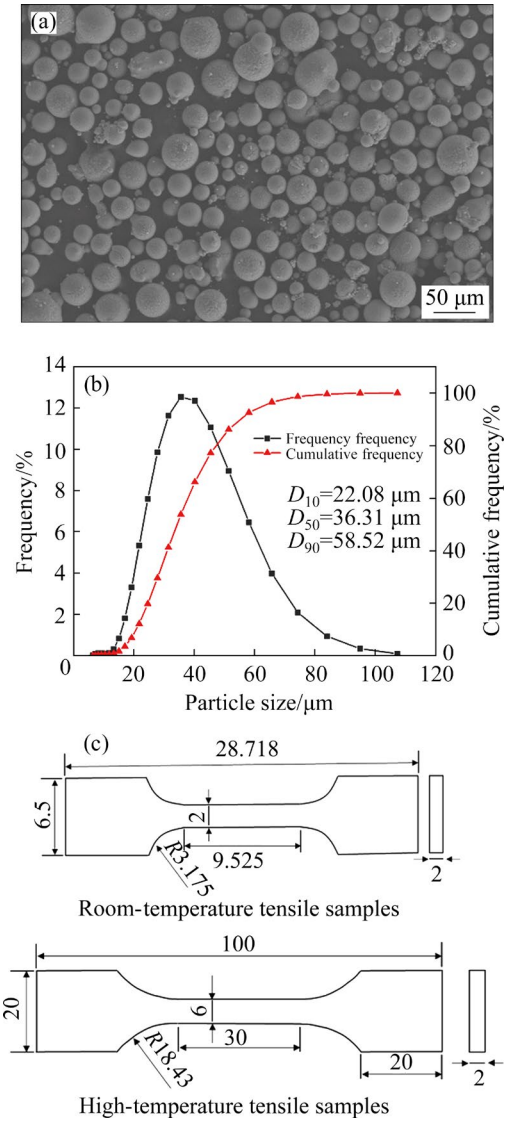

Fig. 1 (a, b) Morphology and particle size distribution of prepared powder, respectively; (c) Dimensions of room-temperature and high-temperature tensile sheets (Unit: mm)

As for the PBF-LB samples, after mechanical polishing with 3000# sandpaper, electrochemical polishing was conducted using a 90 vol.% C_2H_5OH and 10 vol.% $HClO_4$ solution. Microstructural analysis was conducted using an optical microscope (OM, Zeiss-Image) and a scanning electron microscope (SEM, Zeiss Sigma 300).

Electron back-scattered diffraction (EBSD) analysis was performed to determine the crystallographic orientation and grain size of the PBF-LB printed samples. The samples were prepared by using a three-axis ion beam polishing instrument (Leica EM TIC 3X). The EBSD system used was an Oxford Instruments Nordlys Nano EBSD detector in conjunction with a Tescan AZtec software.

The nanoscale precipitates were observed using a transmission electron microscope (FEI Tecnai G2−F30) operating at 200 kV. The TEM specimens were sliced in a direction parallel to the PBF-LB printing direction, mechanically ground to a thickness of 30 μm, punched into 3 mm diameter disks, and further thinned using an ion milling system (Gatan 695) to produce electron transparent areas.

Structural analysis was performed by X-ray diffraction (XRD) using an X'Pert PRO instrument with Cu K_α radiation (λ=1.5406 Å) at a scanning speed of 2 (°)/min.

The hardness of the specimens was assessed using an HSV−1000 Vickers hardness machine. The measurements were taken with an external load of 200 g and a dwell time of 10 s. The mean value was obtained from 5−10 points on each specimen to ensure the accuracy of the data.

Tensile properties of the PBF-LB specimens were evaluated by using an AGS-X electronic universal testing machine. The dimensions of the tensile specimens were illustrated in Fig. 1(c). The crosshead speed was kept constant at 1 mm/min, and the room-temperature and high-temperature tensile tests were conducted in accordance with the standards GB/T 228.1 and GB/T 228.2, respectively. Prior to the high-temperature tensile testing, the specimens were subjected to 300 °C for an insulation period of 10 min. To ensure the accuracy of the obtained tensile data, the average value of the results from three tensile tests was reported.

3 Results and discussion

3.1 Microstructure of designed alloys

Figure 2 shows the cross-sectional microstructure of the designed nine as-cast alloys after laser remelting. As shown in Figs. 2(a−i), no obvious metallurgical defects were observed. Meanwhile, the as-cast and laser-remelted regions exhibited distinct microstructures. As shown in Fig. 2(e), the cast region displayed α-Al dendrites, needle-like eutectic Si, and blocky primary Fe-containing secondary phase particles. However, as shown in Fig. 2(h), the remelted heat-affected zone still contained unmelted blocky primary Fe-containing phases, which subsequently underwent

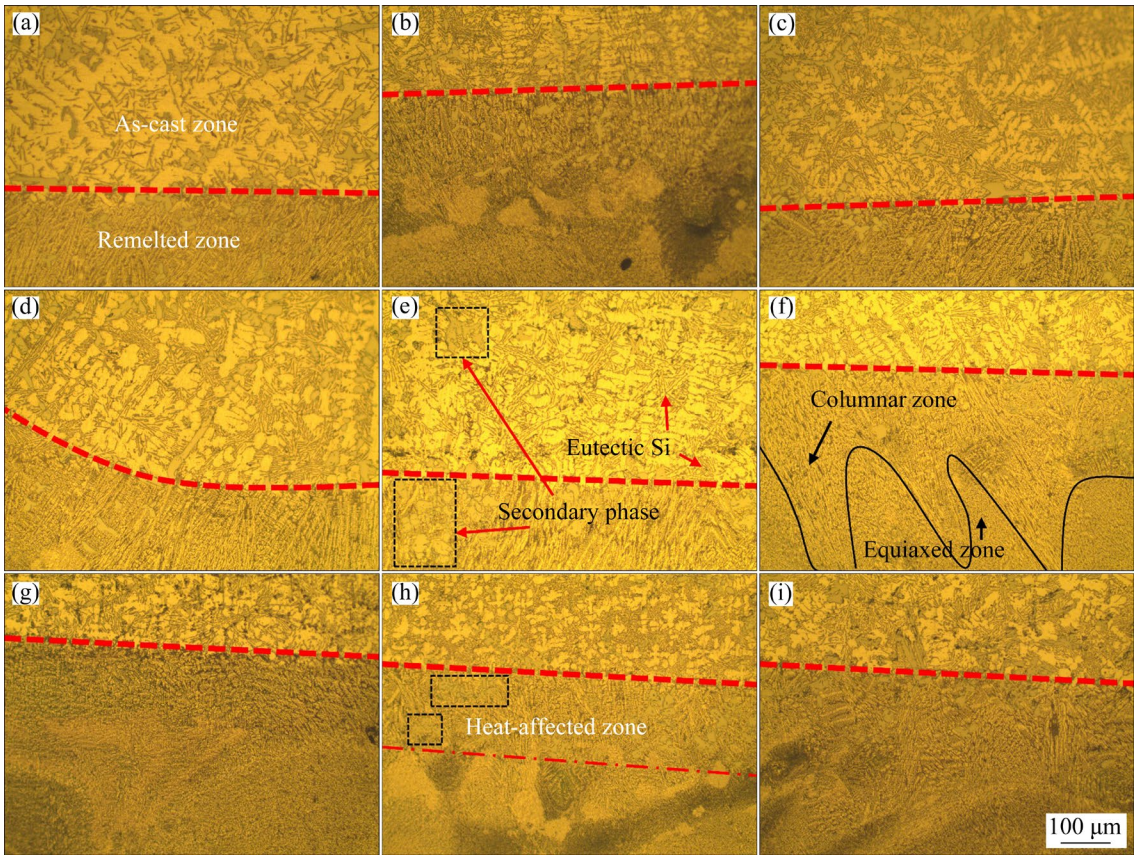

Fig. 2 Optical micrographs of different as-cast alloys after laser remelting: (a) 1# alloy; (b) 2# alloy; (c) 3# alloy; (d) 4# alloy; (e) 5# alloy; (f) 6# alloy; (g) 7# alloy; (h) 8# alloy; (i) 9# alloy

complete melting as they traversed the edge of the heat-affected zone, approaching the center of the remelted zone. This phenomenon was due to the Gaussian heat source distribution of the laser, resulting in a high temperature at the center and lower temperatures on both sides [20]. The microstructure of the laser-remelted region exhibited a notable degree of refinement, manifesting as fine cellular structures. Besides, in the heat-affected zone, the coarse secondary phase particles were fully melted. Additionally, as shown in Fig. 2(f), the laser-remelted region exhibited columnar and equiaxed crystal zones. The main reason for the distinct microstructures was the considerably high cooling rate during laser remelting compared to that during casting. Subsequently, the solidification cells and equiaxed dendrites underwent a significant degree of refinement in the remelted zone.

Figure 3 shows the SEM−EDS images of the as-cast and remelted regions of 1# alloy. The SEM−EDS images of the as-cast area in Figs. 3(a−g) provided further validation of the secondary phase species identified in Fig. 2(e). These images confirmed the presence of needle-like eutectic Si, α-Al(FeMn)Si, and Al−Ni phases. As shown in Fig. 3(h), after laser remelting, the previously observed coarse primary phases were observed to melt and disappear, with the equiaxial crystal region comprising a grey α-Al matrix and the white reticular Si. This microstructure was similar to that typically observed in the PBF-LB formed Al−Si alloys [21], which indicated that the laser remelting process was feasible. This process provided sufficient energy density for remelting and sufficiently rapid cooling rates to facilitate the melting and recombination of the eutectic Si and Fe-containing phases. Therefore, the formation of undesirable phases, such as coarse Fe-containing phases, was effectively inhibited by the relatively rapid cooling of PBF-LB during the preparation of Al−Si−Fe alloys.

Figure 4 shows the remelted equiaxed crystal zones of 1#, 2#, and 5# alloys with increasing the Ni content from 0.4 wt.% to 1.2 wt.%. It can be observed that the grain size became gradually

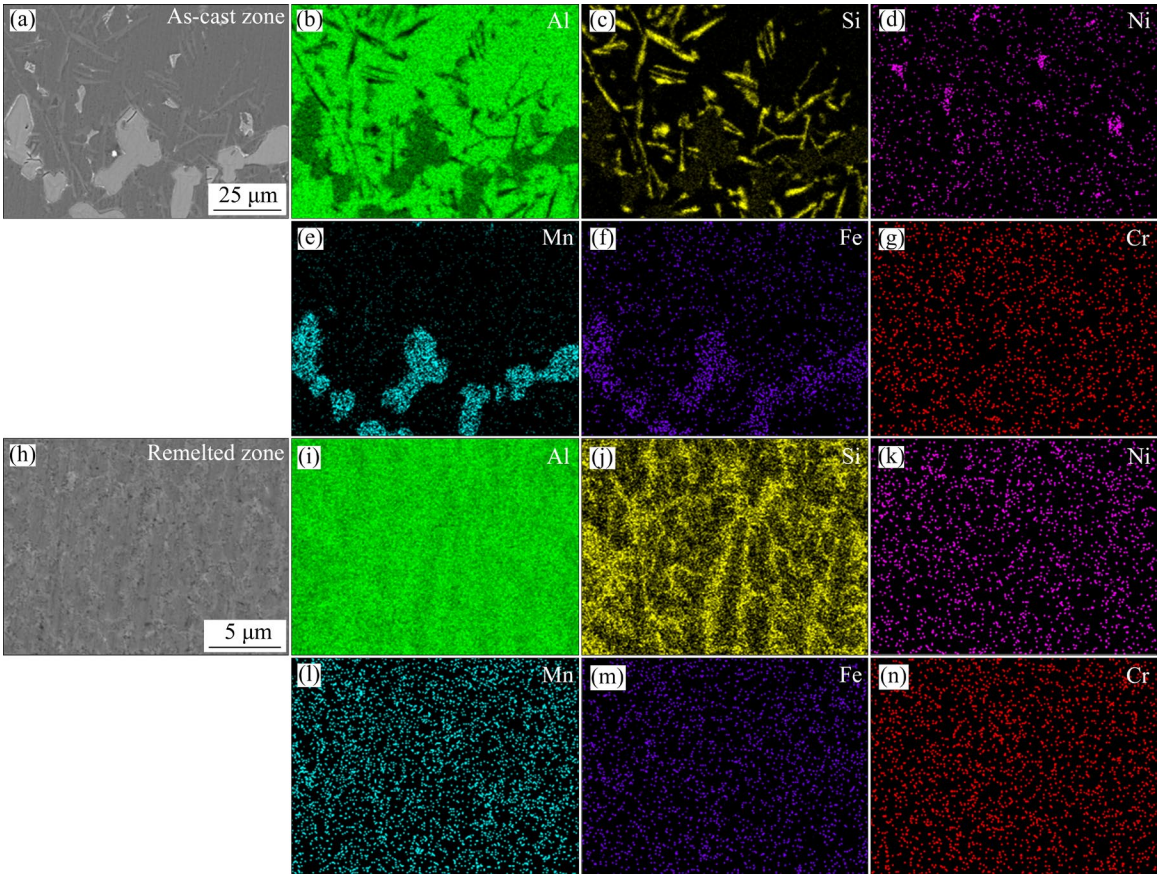

Fig. 3 SEM−EDS images of 1# alloy: (a−g) As-cast region; (h−n) Remelted region

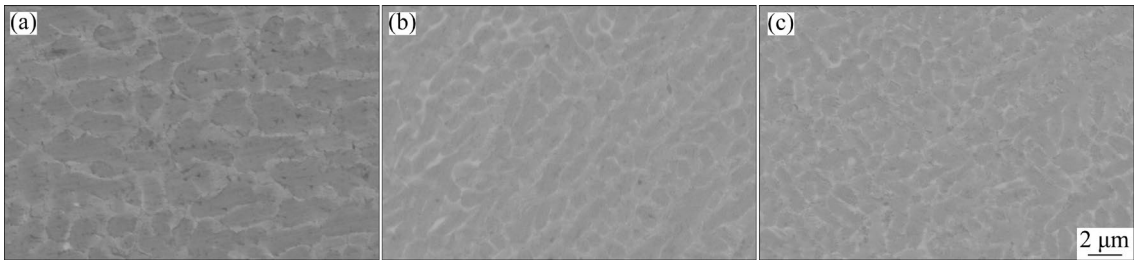

Fig. 4 SEM−BSE images of remelted equiaxed crystal zones of different alloys after remelting: (a) 1# alloy; (b) 2# alloy; (c) 5# alloy

refined, measuring 2.66, 1.87, and 1.72 μm, respectively. The main difference among these alloys was the Ni content. It can be inferred that the formed Al_3Ni phase acted as a non-homogeneous phase nucleator, thereby controlling the microstructure at high cooling rates [22]. In the PBF-LB process, significant thermal gradients and high cooling rates could result in a coarse columnar crystal structure, which may lead to the anisotropy in the mechanical properties and an increased susceptibility to cracking [2]. The obtained fine equiaxial microstructure exhibited enhanced mechanical properties and increased resistance to cracking. Additionally, Ni has the capacity to destabilize the β-$Al_9Fe_2Si_2$ phase and promote the formation of the high-strength and heat-resistant Al_9FeNi phase [23]. However, an excessive amount of Ni could lead to the transformation of the Al_9FeNi phase into long needle-like structures, which may have a detrimental impact on the mechanical properties of the aluminum matrix.

3.2 Microhardness and orthogonal analysis results

Figure 5 shows the microhardness of the as-cast and remelted regions of the designed nine alloys. As shown in Fig. 5, the microhardness of the

remelted zone was significantly higher than that of the as-cast zone. In the remelted zone, 2# alloy exhibited the highest microhardness of $HV_{0.2}$ (152.8±4.15), while 8# alloy demonstrated the lowest value of $HV_{0.2}$ (129±3.53). Table 2 presents the results of the orthogonal microhardness experiments in the remelted zone. Each factor has three experiments at the same level, and the three microhardness results obtained with the same factor level were then added together to obtain K_1, K_2, and K_3. The range (R) was calculated as the difference between the maximum and minimum K values. This reflected the impact of the selected levels of elements on the microhardness. According to Table 2, the impact levels followed R(Cr)>R(Ni)>R(Mn)>R(Fe), indicating that Cr had the most significant influence on the microhardness of the alloy, followed by Ni, Mn, and Fe.

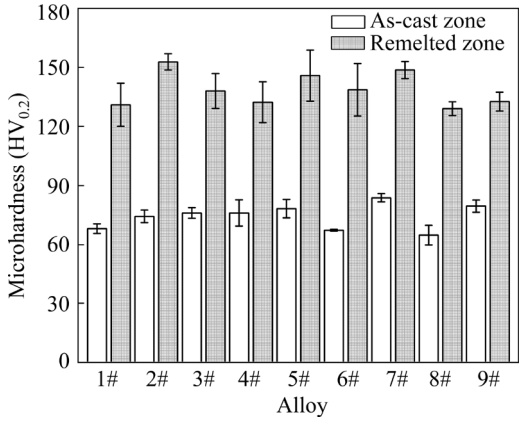

Fig. 5 Microhardness of as-cast and remelted zones of different alloys

Table 2 Orthogonal experimental results in remelted region

Alloy	Content/wt.%				Microhardness ($HV_{0.2}$)
	A(Fe)	B(Mn)	C(Ni)	D(Cr)	
1#	2.5	1.5	0.4	0.2	131.00±10.94
2#	2.5	2.0	0.8	0.4	152.80±4.15
3#	2.5	2.5	1.2	0.6	138.00±8.86
4#	3.0	1.5	0.8	0.6	132.33±10.39
5#	3.0	2.0	1.2	0.2	145.80±12.99
6#	3.0	2.5	0.4	0.4	138.60±13.33
7#	3.5	1.5	1.2	0.4	148.67±4.32
8#	3.5	2.0	0.4	0.6	129.00±3.54
9#	3.5	2.5	0.8	0.2	132.60±4.77
K_1	421.80	412.00	398.60	409.40	
K_2	416.73	427.60	417.73	440.07	
K_3	410.27	409.20	432.47	399.33	
R	11.53	18.40	33.87	40.74	

The orthogonal results indicate that the increase in microhardness observed in the remelted zone could be attributed primarily to the controlling effect of the Cr and Mn elements on the morphology of the Fe-containing phases. Furthermore, the microhardness is further improved by the diffuse distribution of melt-reorganized α-Al(FeMn)Si and Ni-containing phases, which are governed by Marangoni driven fluid flow (as evidenced by different color linings of the remelted zone in Fig. 2) in the molten pool. Furthermore, the addition of Ni contributed to the grain refinement. According to the Hall−Petch relationship, the grain refinement had a positive impact on improving the mechanical properties. In summary, the optimal alloy composition was determined as Al−11Si−2.5Fe−2Mn−1.2Ni−0.4Cr.

4 PBF-LB manufacturing and verification

4.1 Microstructure of PBF-LB manufactured Al−Si−Fe alloy

Vacuum gas atomized powder preparation was carried out based on the optimized alloy composition. Subsequently, PBF-LB was implemented using the optimized process parameters. The XRD pattern of the PBF-LB manufactured Al−Si−Fe alloy is shown in Fig. 6. According to the XRD spectrum, the alloy mainly consisted of three phases, which were α-Al, Si, and α-Fe phase ($Al_{17}Fe_{3.2}Mn_{0.8}Si_2$). However, the Cr- and Ni-containing phases were not identified in the XRD pattern.

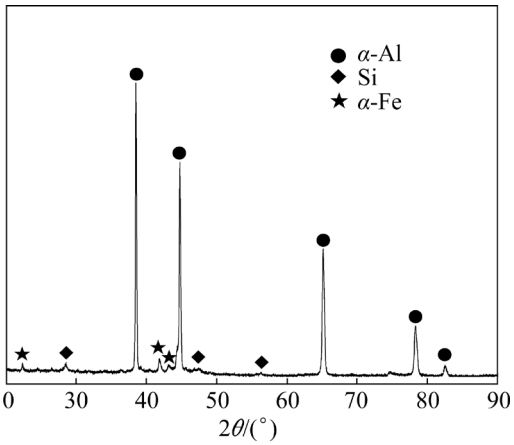

Fig. 6 XRD pattern of PBF-LB manufactured Al−Si−Fe alloy

Figure 7(a) shows the cross-section microstructure of the PBF-LB manufactured alloy, revealing a typical fish-scale-like molten pool structure. Good metallurgical bonding was observed between the layers of the molten pool, with irregular angles and arrangements between the molten pools. This was due to the scanning strategy, which involved a certain angular deviation. No cracks or other significant defects were observed in the PBF-LB manufactured alloy. The microstructure was observed to be dense, with an alloy density of 99.8%, as measured by the Archimedes method. This finding demonstrates good PBF-LB processability of the alloy. Figure 7(b) shows an enlarged view of the molten pool boundaries, which exhibits a distinctive intermetallic morphology. It comprises the classical grey α-Al phase and a continuous distribution of white secondary phase along the grain boundaries. Compared to the α-Al structure observed after laser remelting, as shown in Fig. 4(c), the PBF-LB manufactured sample exhibited a more refined microstructure due to the elevated cooling rates. The table in Fig. 7 shows the EDS results of the spherical particle phases at the molten pool boundaries and the white secondary phase in Fig. 7(b). The results obtained at Spot 1 indicated that the secondary phase was primarily composed of Fe-rich phases, while at Spot 2, the

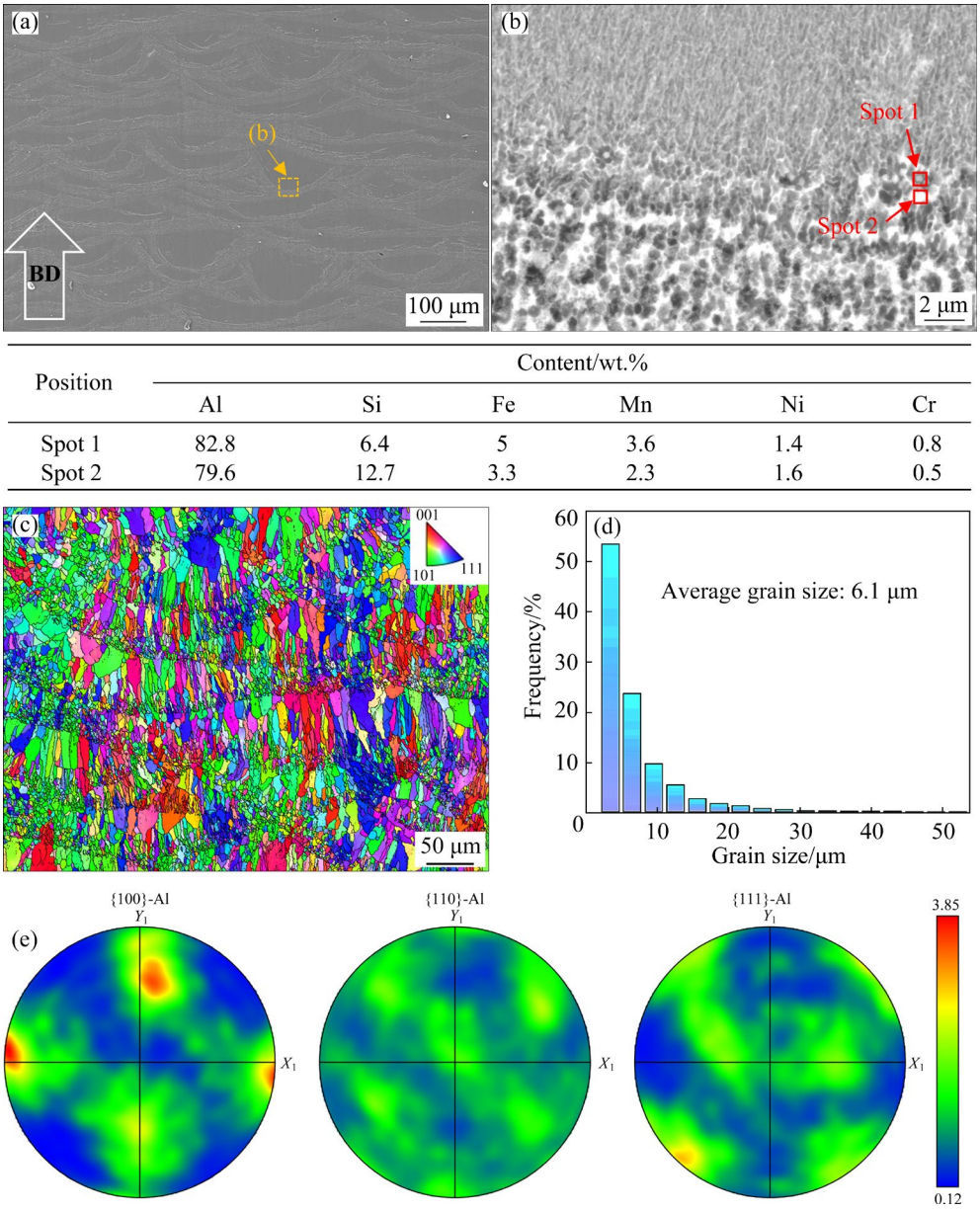

Position	Content/wt.%					
	Al	Si	Fe	Mn	Ni	Cr
Spot 1	82.8	6.4	5	3.6	1.4	0.8
Spot 2	79.6	12.7	3.3	2.3	1.6	0.5

Fig. 7 Microstructures of PBF-LB manufactured Al−Si−Fe alloy: (a) SEM image; (b) Enlarged view of red-framed area in (a); (c) EBSD image; (d) Grain size distribution; (e) Pole figures

white phase was enriched in Si compared to the spherical particles. The two structures merged to create a secondary phase enriched zone at the molten pool boundary. In some reported PBF-LB fabricated Al−Si alloys [8,24], a cellular aluminum matrix was surrounded by spherical eutectic silicon particles, forming a eutectic silicon network. However, in this study, it was found that Si was more likely to form a secondary phase with Fe, Mn, and other elements, which were distributed around the aluminum matrix, as indicated by the XRD and EDS results in Fig. 7, due to the elevated alloying element content.

As illustrated in Fig. 7(c), the EBSD image reveals that the Al−Si−Fe alloy was composed of columnar crystals (CG) in the middle of the molten pool and equiaxed fine grains (FG) at the bottom of the molten pool. This was primarily attributed to the uneven heat distribution caused by the Gaussian distribution of the laser heat source. The relevant solidification phenomena were determined by the thermal gradient and the solid−liquid interface solidification velocity [12,25]. At the bottom of the molten pool, the solidification velocity was relatively low. As a consequence of the layer-by-layer scanning process employed in PBF-LB, the upper surface of the previous molten pool was remelted, resulting in the formation of fine equiaxed crystals. These grains, with sizes ranging from 2 to 5 μm, constituted 53.4% of the total, as shown in Fig. 7(d). In the middle of the molten pool, the formation of columnar crystals was observed as a consequence of a reduction in the thermal gradient and an increase in the solidification rate. To examine the orientation of the grains, pole figure analysis was conducted. According to the pole figures shown in Fig. 7(e), the pole density ranged from 0.12 to 3.85, indicating a relatively weak texture in the PBF-LB fabricated alloy, with a random growth direction of the grains.

Figure 8 shows the TEM images of the molten pool in the Al−Si−Fe alloy. As shown in Fig. 8(a), the presence of columnar crystal regions and equiaxed fine grain regions (secondary phase enriched regions) were present. As illustrated in Fig. 8(d), the columnar crystalline region consisted of a Si-rich cytosolic structure, while the aluminum matrix in this region exhibited a reduced number of nucleation sites and a more pronounced solidification thermal gradient. These factors collectively contributed to the formation of the columnar crystal region. The secondary phase enriched zone at the bottom of the molten pool was mainly composed of submicron-scale nearly-equiaxed blocky phases and nanometer-scale spherical phases. The blocky phase was distributed both within and along the boundaries of the grains, while the nanoscale spherical phase was mainly distributed along the grain boundaries. According to the corresponding EDS maps, these blocky intermetallic phases were rich in Al, Si, Fe, Mn, Ni, and Cr. EDS and diffraction spot analyses were performed on the blocky phases, as shown in Fig. 8(b). Based on the TEM diffraction pattern, this phase was confirmed as the $Al_{17}Fe_{3.2}Mn_{0.8}Si_2$-type phase. However, according to the EDS results in Fig. 8(b), this phase was close to $Al_{17}(FeMnNiCr)_4Si_2$. It is observed that, due to the similarity in atomic radii, the substitution of Fe or Mn by Ni and Cr did not lead to crystal distortion. A similar situation was reported in nearly-eutectic and subeutectic Al−Si−Ni−Fe−Mn alloys produced by die casting [26]. This finding corroborates the hypothesis that the morphology of the α-Fe phase could be manipulated by the incorporation of Mn, Ni, and Cr elements.

Figure 9(a) shows the local morphology of the secondary phase enriched zone. High-resolution TEM (HRTEM) and Fourier transform (FFT) analyses were conducted on the nanoscale spherical phase depicted in Figs. 9(b, c). These analyses revealed that the precipitated phase was α-Al(FeMn)Si, with a size of 50−90 nm. The distribution of the two precipitated phases within the molten pool was uneven, with the majority located at the molten pool boundaries and a small portion distributed in the middle of the molten pool. The formation of the initial molten pool resulted in a high thermal gradient at the boundaries, which initiated the solidification process and led to the formation of primary phases such as α-Fe and α-Al(FeMn)Si. As shown in Fig. 9, the semi-congruent interfaces of α-Al(FeMn)Si and α-Al are almost overlapped, indicating that the α-Al(FeMn)Si phase existed as a nucleation site. Furthermore, when the laser remelted the previous molten pool, the primary phases were not completely melted, acting as nucleation sites within the liquid phase. This resulted in the formation of the secondary phase enriched zone and the refinement

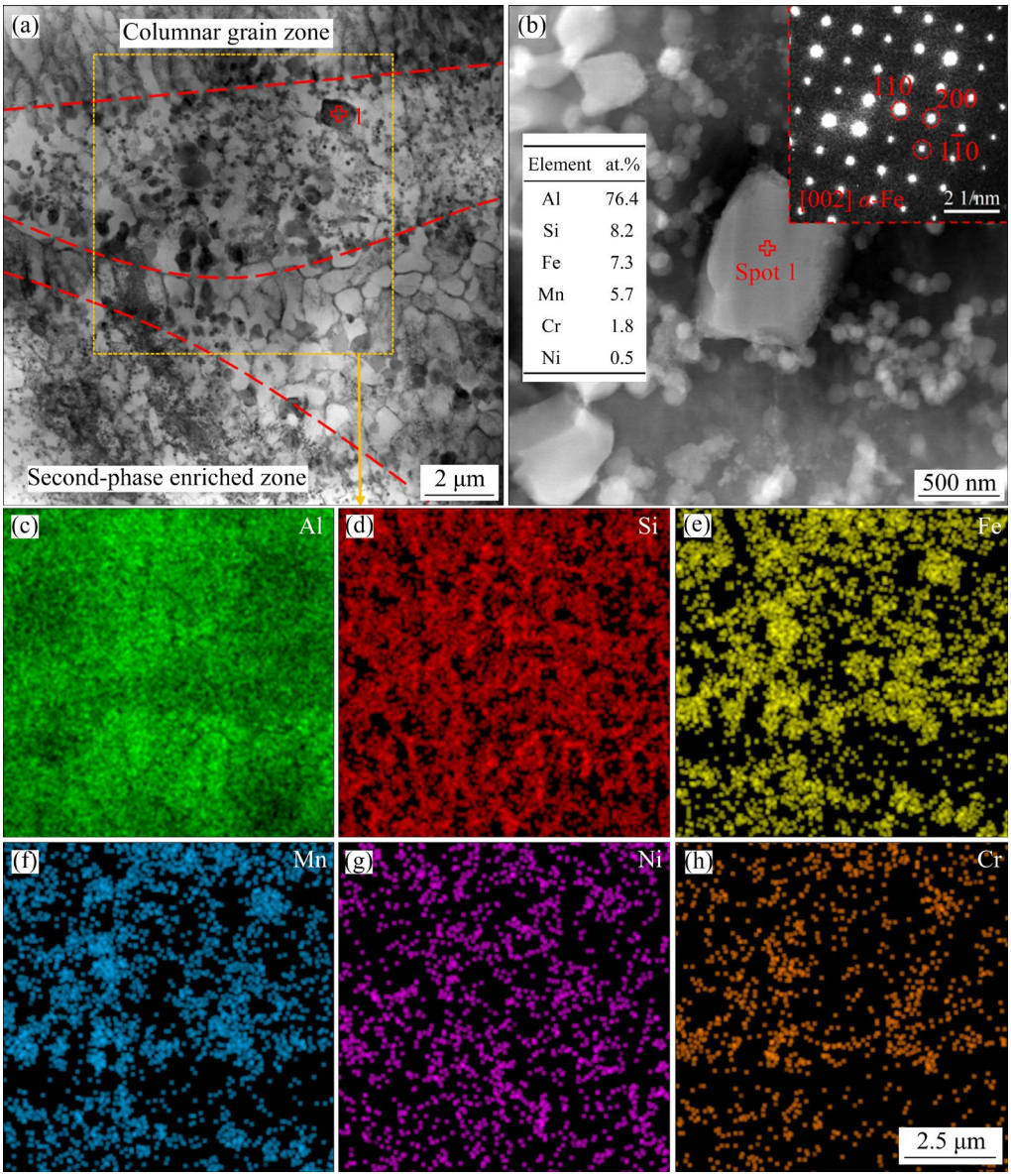

Fig. 8 TEM images showing molten pool morphology of PBF-LB manufactured Al−Si−Fe alloy: (a) Bright-field TEM image; (b) Dark-field TEM image and EDS results from Point 1 in (a) and diffraction pattern of Spot 1; (c−h) EDS maps corresponding to yellow box in (a)

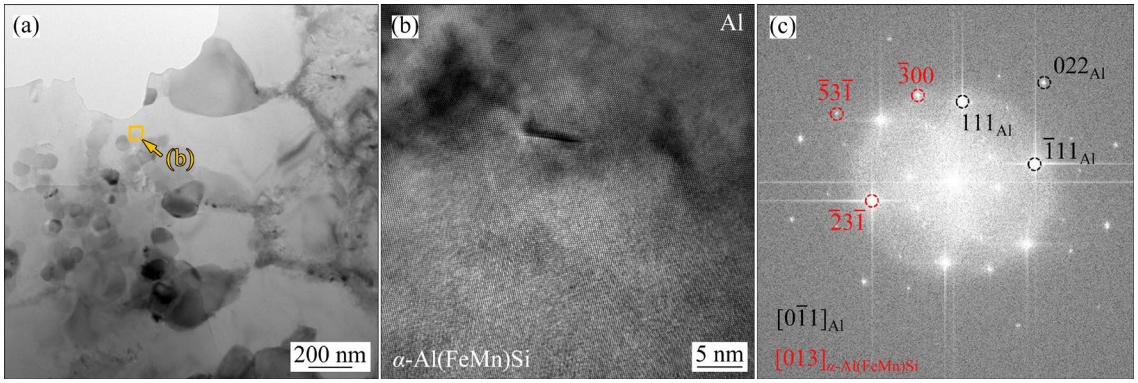

Fig. 9 (a) Bright-field TEM image showing local morphology of secondary phase enriched region; (b) HRTEM image revealing interface between Al and α-Al(FeMn)Si; (c) Fourier transform results of (b)

of grains. As the process of solidification continued, a decrease in the thermal gradient was observed, accompanied by an increase in the solidification velocity. Under these conditions, the formation of the two Fe-containing primary phases appeared to be suppressed, as evidenced by the sparse presence of these phases in the columnar crystal zone in Fig. 8(a). The presence of minor quantity of the α-Fe phase did not function as a nucleation site for α-Al, presumably because the localized solidification conditions prevented nucleation conditions. Moreover, the depletion of the primary phases resulted in a reduction in nucleation sites, which in turn led to the coarsening of α-Al grains in the central region of the molten pool. Additionally, analogous microstructural characteristics have also been reported in PBF-LB manufactured Al−3.6Mn−2.0Fe−1.8Si−0.9Zr (wt.%) alloy [17].

Besides the two Fe-containing primary phases, Al−Ni phases were observed in the as-cast zone in Fig. 3(d), which were not identified in the TEM observations of the PBF-LB manufactured alloy. It has been demonstrated that in the Al−Si−Fe−Ni−Mn system, a quaternary eutectic reaction occurs under near-equilibrium conditions, whereby the liquid phase transforms to α-Al+Si+Al_3Ni+$Al_9(FeNiMn)_2$. When the solidification process occurs rapidly, such as in high-pressure die casting (HPDC), this reaction transforms from the liquid phase to α-Al+Si+Al_6(FeNiMn) at 567 °C [26]. In this study, neither the Al_3Ni phase under equilibrium solidification conditions nor the Al_6(FeNiMn) phase under rapid solidification conditions was observed. It was speculated that the faster solidification conditions of the PBF-LB process kinetically inhibited the formation of these two phases. In this work, the incorporation of Ni element into the primary Fe-containing phases resulted in the formation of Al(TM)Si phases, rather than the generation of an excess amount of intermetallic compounds. This finding is in consistent with previous reports on aluminum alloys with the addition of transition metal elements [27−29], including Mn, Fe, Ni, Cr, V, etc.

4.2 Mechanical properties of PBF-LB manufactured Al−Si−Fe alloy

The average microhardness of the PBF-LB manufactured Al−Si−Fe alloy on the *XOY* plane or cross-section, was $HV_{0.2}$ (171.08±5.36), while on the *XOZ* plane or longitudinal section, a value of $HV_{0.2}$ (144.64±4.52) was obtained. Figure 10 illustrates the tensile properties of the PBF-LB manufactured alloy. As shown in Fig. 10(a), the room-temperature yield strength (YS), ultimate tensile strength (UTS) and elongation to fracture (EL) of the PBF-LB manufactured Al−Si−Fe alloy were (337.79±2.36) MPa, (512.76±3.26) MPa and

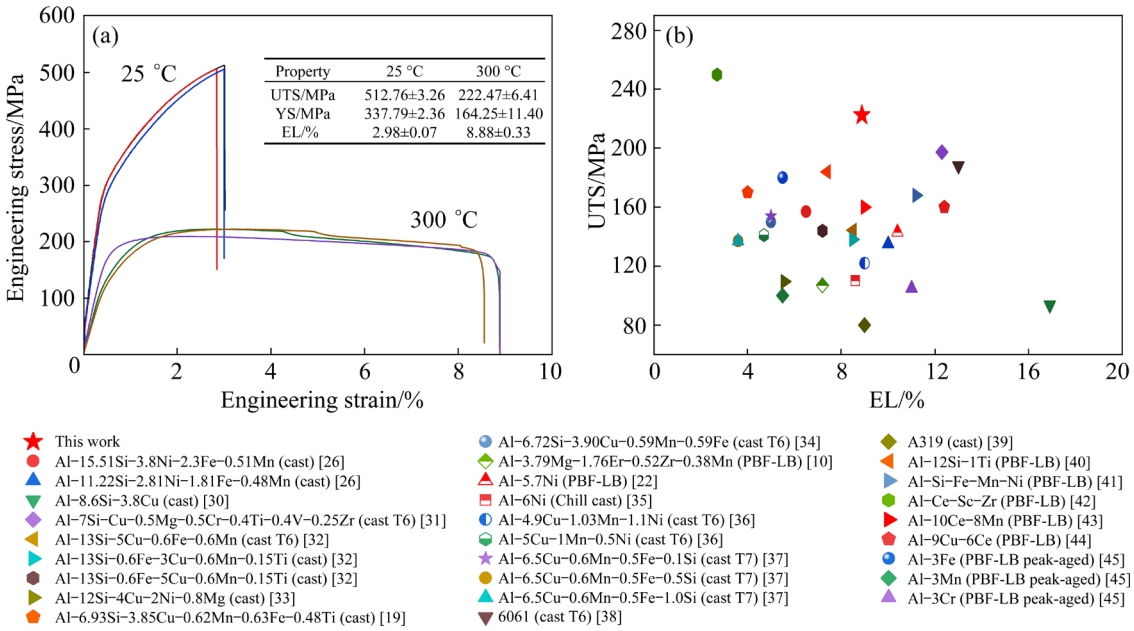

Fig. 10 (a) Room-temperature and high-temperature (300 °C) tensile properties of PBF-LB manufactured Al−Si−Fe alloys; (b) Comparison of high-temperature tensile performance at 300 °C between this work and other as-cast or PBF-LB manufactured Al−Si and Al−Cu alloys [10,19,22,30−45]

(2.98±0.07)%, respectively. Compared to the commonly PBF-LB manufactured AlSi10Mg alloys [29], the Al−Si−Fe alloy in this research exhibited a higher room-temperature YS. The results of the high-temperature tensile testing, conducted at 300 °C, showed a UTS of (222.47±6.41) MPa and an EL of (8.88±0.33)%, as shown in Fig. 10(a). A comparison of high-temperature tensile testing at 300 °C was obtained using commercially available alloys, including as-cast Al−Si alloy, Al−Cu alloy, and A319 alloy [10,13,19,22,30−45], which clearly indicated that the PBF-LB manufactured Al−Si−Fe alloy demonstrated a superior combination of high-temperature strength and ductility.

Figure 11 illustrates the fracture surfaces of the specimens after room-temperature and high-temperature tensile testing. As shown in Fig. 11(a), the presence of extensive disintegrated surfaces was observed in the flat region, along with the presence of small pores in its vicinity, followed by a shallower portion of tear ridges. This indicated that the cracks initiated from the pore regions at the edge of the specimen and rapidly propagated across the entire cross-section after plastic deformation, ultimately leading to the fracture. The existence of pores was observed as a common defect in the PBF-LB processing of aluminum alloys, due to the entrapment of unmelted powder or metal vapor and protective gas in the molten pool [46]. Figure 11(b) shows a high-magnification view in Fig. 11(a), demonstrating relatively shallow and small dimples morphology, which corresponded to the lower elongation at room-temperature, indicating brittle fracture. The fracture surface of the specimen tested at 300 °C revealed ductile fracture, with numerous large dimples, as shown in Figs. 11(c, d). Compared to the room-temperature fracture surface, the dimples were larger and deeper, reflecting a better toughness. Additionally, at the bottom of the dimples, the presence of significant secondary phase

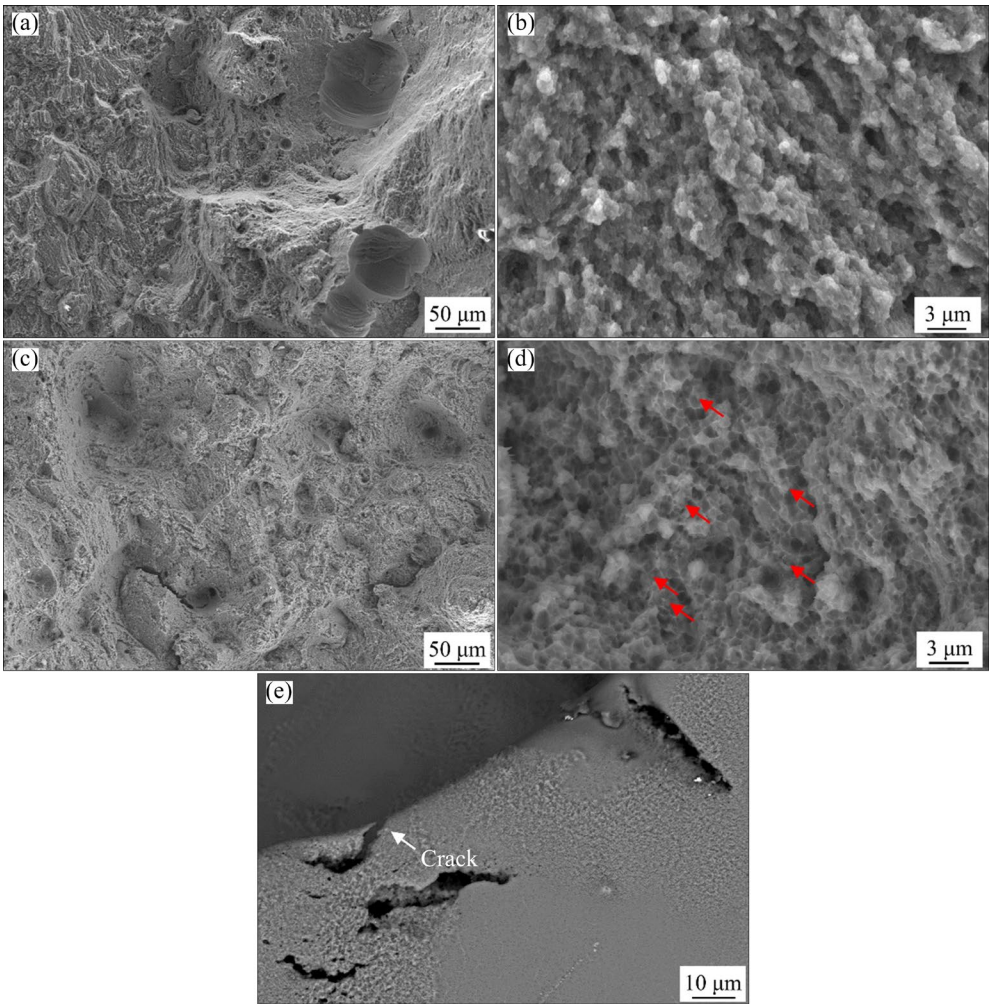

Fig. 11 Fracture surfaces of PBF-LB manufactured Al−Si−Fe alloys: (a, b) At room temperature; (c−e) At high temperature of 300 °C

particles indicated that the secondary phase acted as nucleation sites for the dimples. Figure 11(e) shows the side fracture of an Al−Si−Fe alloy at a high temperature of 300 °C. It can be found that the cracks originated and occurred in the secondary phase enriched zone, indicating that this region was loaded during high temperature stretching.

The primary room-temperature strengthening mechanisms of this alloy were as follows: fine-grain strengthening within the equiaxial crystal zone; solid solution strengthening due to the high solubility of the elements in the Al matrix; precipitation strengthening resulting from the generation of multiple phases due to the high content of alloying elements. In contrast to equilibrium solidification, the solubility of the Fe element in Al alloys could be significantly enhanced during laser rapid solidification [47]. Similarly, the solubility of Si element in α-Al could reach about 7% in PBF-LB manufactured Al alloys [48]. The Al−Si−Fe alloys exhibited good tensile strength as a result of the combined action of multiple strengthening mechanisms. However, as illustrated in Figs. 8(a, b), the microstructure of the sample reveals that the aluminum matrix in the Al−Si−Fe alloys was compartmentalized by a network of heat-resistant phases, forming fine cell-like structures. This morphology impeded the movement of dislocations and shortened the path of dislocation slip, thereby hindering the transfer of dislocations between cells. Furthermore, the interconnected boundaries of the molten pool, comprising the hard heat-resistant phases impeded the plastic deformation of the aluminum matrix during stretching, thereby conferring relatively low ductility.

When the temperature reached $0.5T_m$ (T_m is the melting point), the grain boundaries exhibited softening, thereby rendering fine-grain strengthening inapplicable [49]. Thus, aluminum alloys with softened grain boundaries were susceptible to sliding and rotation at elevated temperatures [34]. Therefore, the high-temperature strength mainly came from the presence of high-temperature strengthening phases. According to TEM analysis in Fig. 8, a significant amount of strengthening phases, such as α-Fe and α-Al(FeMn)Si, were distributed at the grain boundaries and within the grains. During high-temperature tensile loading, these phases could act as pinning agents at the grain boundaries, hindering the motion and slip of grain boundaries. The thermal stability of the α-Al(FeMn)Si phase was previously documented. In PBF-LB preparation of the Al−3.6Mn−2.0Fe−1.8Si−0.9Zr (wt.%) alloy, after subsequently aging at 350 °C for 8 h, the high hardness of the alloy was mainly attributable to the presence of α-Al(FeMn)Si precipitates. Furthermore, the high volume fractions of thermally stabilized α-Al(FeMn)Si phases resulted in the alloy exhibiting excellent high-temperature creep resistance [17].

Another important factor affecting the high-temperature performance of aluminum alloys was the coarsening of the secondary phase and the occurrence of phase transformation at elevated temperatures [19]. In this study, α-Fe and α-Al(FeMn)Si, which are heat-resistant phases, contain a significant number of transition group elements with low diffusivity at high temperatures. This effectively reduces phase coarsening. The skeleton structure, comprising thermally stable intermetallic phases, is also capable of effectively anchoring grain boundaries at high-temperatures, thereby suppressing the grain boundary migration and sliding [49,50]. As shown in Fig. 12, the secondary phase enriched regions were located at the molten pool boundaries, appearing as white reticular structures in the SEM microstructures depicted in Fig. 7(a). The processing characteristics of PBF-LB resulted in the formation of scale-like interconnected structures at the boundaries of the molten pool. Therefore, under high-temperature stress, although the aluminum matrix softened, the

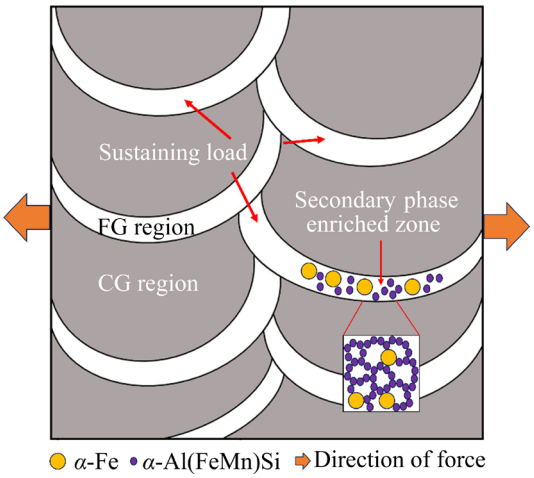

Fig. 12 High-temperature strengthening mechanism of developed Al−Si−Fe alloy

three-dimensional reticular structure formed by the secondary phase enriched zone acted as a skeleton structure, bearing the load and ensuring high-temperature strength. The cracks observed in the secondary phase enriched zone in Fig. 11(e) proved that this region was responsible for bearing loads at high temperatures.

5 Conclusions

(1) After laser remelting, the needle-like eutectic Si structures within the as-cast Al−Si−Fe alloy transformed into the Si network, and the blocky primary Fe-rich phase completely melted in the central area of the remelted region. The orthogonal experiment results indicated that the addition of Cr and Mn elements and their contents had the greatest impact on the hardness of the remelted zone. After comprehensive analysis, the optimal alloy composition was determined to be Al−11Si−2.5Fe−2Mn−1.2Ni−0.4Cr(wt.%).

(2) The Al−Si−Fe alloy was prepared by PBF-LB, indicating that the PBF-LB manufactured alloy exhibited a density of 99.8% with discernible defects and a bimodal structure. The molten pool boundaries were primarily composed of submicron-scale α-Fe ($Al_{17}(FeMnNiCr)_4Si_2$) and nanometer-scale α-Al(FeMn)Si phases.

(3) The room-temperature ultimate tensile strength of the PBF-LB manufactured Al−Si−Fe alloy reached (512.76±3.26) MPa, with a yield strength of (337.79±2.36) MPa and an elongation of (2.98±0.07)%. The enhanced room-temperature mechanical properties resulted from the combined effects of fine-grain strengthening at the molten pool boundary, solid solution strengthening of the alloying elements, and precipitation strengthening brought about by the precipitated phases.

(4) At 300 °C, the high-temperature ultimate tensile strength was (222.47±6.41) MPa, with a yield strength of (164.25±11.40) MPa and an elongation of (8.88±0.33)%, exhibiting a superior combination of high-temperature strength and ductility over previously reported alloys. The improved high- temperature mechanical properties were primarily attributable to the three-dimensional skeletal network, comprising the α-Fe and α-Al(FeMn)Si heat-resistant phases at the molten pool boundary and the two heat-resistant phases, which were markedly refined and distributed in a cellular manner. These phases served as anchors at the grain boundaries.

CRediT authorship contribution statement

Wen-zhe GAO: Investigation, Methodology, Writing − Original draft; **Li ZHANG:** Conceptualization, Formal analysis, Resources, Writing − Review & editing; **Kai-yang LI:** Validation; **Xiao-hui YANG:** Resources, Visualization; **Jin-fang ZHANG:** Data curation; **Jian-hong WANG:** Software, Visualization; **Hong XU:** Software, Visualization; **Pei-kang BAI:** Resources, Visualization; **Yuan-kui CAO:** Formal analysis, Validation; **Bin LIU:** Conceptualization, Supervision; **Xiao-feng LI:** Funding acquisition, Supervision, Writing − Review & editing.

Declaration of competing interest

The authors declare that they have no known competing financial interests or personal relationships that could have appeared to influence the work reported in this paper.

Acknowledgments

This work was financially supported by the National Natural Science Foundation of China (Nos. 52375393, 52071299), the Science and Technology Innovation Talent Team of Shanxi Province, China (No. 202304051001029), the Scientific and Technological Achievements Transformation Guidance Project of Shanxi Province, China (No. 202204021301048), the Key R&D Program of Shanxi Province, China (Nos. 2210300058MZ, 202202150401020), the Hai'an & Taiyuan University of Technology Advanced Manufacturing and Intelligent Equipment Industrial Research Institute, China (No. 2023HA-TYUTKFYF020), and the Young Elite Scientists Sponsorship Program by CAST, China (No. 2023QNRC001).

References

[1] WANG Zhen-hong, ZHANG Li-tong, SU Bin, ZHANG Xiao-peng. Simulation on microstructure evolution of Al−Si alloy under effect of natural convection during solidification [J]. Transactions of Nonferrous Metals Society of China, 2022, 32(1): 79−90.

[2] ABOULKHAIR N T, SIMONELLI M, PARRY L, ASHCROFT I, TUCK C, HAGUE R. 3D printing of aluminium alloys: Additive manufacturing of aluminium alloys using selective laser melting [J]. Progress in Materials Science, 2019, 106: 100578.

[3] KUSOGLU I M, GÖKCE B, BARCIKOWSKI S. Research trends in laser powder bed fusion of Al alloys within the last decade [J]. Additive Manufacturing, 2020, 36: 101489.

[4] HYER H, ZHOU L, MEHTA A, PARK S, HUYNH T, SONG Shu-tao, Bai Yuan-li, Cho K, MCWILLIAMS B, SOHN Y. Composition-dependent solidification cracking of aluminum−silicon alloys during laser powder bed fusion [J]. Acta Materialia, 2021, 208: 116698.

[5] YAN Qian, SONG Bo, SHI Yu-sheng. Comparative study of performance comparison of AlSi10Mg alloy prepared by selective laser melting and casting [J]. Journal of Materials Science & Technology, 2020, 41: 199−208.

[6] JIA Zhi-hong, ZHOU Guang-wen, ZHOU Hong-yu, LIU Fei, DING Li-peng, WENG Yao-yao, XIANG Kai-yun, ZHAO Hai-dong. Effects of Cu content and heat treatment process on microstructures and mechanical properties of Al−Si−Mg−Mn−*x*Cu cast aluminum alloys [J]. Transactions of Nonferrous Metals Society of China, 2024, 34(3): 737−754.

[7] TAKATA N, LIU M L, KODAIRA H, SUZUKI A, KOBASHI M. Anomalous strengthening by supersaturated solid solutions of selectively laser melted Al−Si-based alloys [J]. Additive Manufacturing, 2020, 33: 101152.

[8] XIAO Yao, LAN Xin-yue, LU Qiang, DU Yong, LI Kai. In-situ evidence for rotation of Si particles with respect to grains in tensile-deformed Al−Si alloys [J]. Transactions of Nonferrous Metals Society of China, 2023, 33(6): 1655−1664.

[9] UZAN N E, SHNECK R, YEHESKEL O, FRAGE N. High-temperature mechanical properties of $AlSi_{10}Mg$ specimens fabricated by additive manufacturing using selective laser melting technologies (AM-SLM) [J]. Additive Manufacturing, 2018, 24: 257−263.

[10] SUN Yi-wei, WANG Jia-long, SHI Yun, FEI Qin-nan, ZHAO Ning-shuang, NI Chao, WU Ji-li, DONG Yin-sheng, DAI Ting, DING Hui, HAO Meng-long. An SLM-processed Er- and Zr-modified Al−Mg alloy: Microstructure and mechanical properties at room and elevated temperatures [J]. Materials Science and Engineering: A, 2023, 883: 145485.

[11] NAGAUMI H, QIN Jian, YU Cheng-bin, WANG Xiao-guo, WANG Lin-sheng. Quantitative analysis of influence of *α*-Al(MnFeCr)Si dispersoids on hot deformation and microstructural evolution of Al−Mg−Si alloys [J]. Transactions of Nonferrous Metals Society of China, 2022, 32(6): 1805−1821.

[12] MICHI R A, PLOTKOWSKI A, SHYAM A, DEHOFF R R, BABU S S. Towards high-temperature applications of aluminum alloys enabled by additive manufacturing [J]. International Materials Reviews, 2022, 67(3): 298−345.

[13] CAI Qing, FANG Chang-ming, LORDAN E, WANG Yun, CHANG I T H, CANTOR B. A novel Al−Si−Ni−Fe near-eutectic alloy for elevated temperature applications [J]. Scripta Materialia, 2023, 237: 115707.

[14] WANG Bing, WANG Jun-sheng, LIU Xin-xiu, LI Quan, LIU Xiao-guang. Uncovering the effects of neutralizing elements (Co, Mn and Cr) on the Fe-rich intermetallic formation in Al−Si−Cu alloys [J]. Materials Science and Engineering: A, 2022, 858(14): 144090.

[15] LIN Bo, LI Hao-yu, XU Rui, ZHAO Yu-liang, XIAO Hua-qiang, TANG Zheng-qiang, LI Shao-bo. Thermal exposure of Al−Si−Cu−Mn−Fe alloys and its contribution to high temperature mechanical properties [J]. Journal of Materials Research and Technology, 2020, 9(2): 1856−1865.

[16] YU Jiang, GENG Yao-xiang, JU Hong-bo, ZHANG Zhi-jie, XU Jun-hua. Crack elimination and strength enhancement mechanisms of selective laser melted Si-modified Al−Mn−Mg−Er−Zr alloy [J]. Transactions of Nonferrous Metals Society of China, 2024, 34(8): 2431−2441.

[17] MANCA D R, CHURYUMOV A Y, POZDNIAKOV A V, RYABOV D K, KOROLEV V A, DAUBARAYTE D K. Novel heat-resistant Al−Si−Ni−Fe alloy manufactured by selective laser melting [J]. Materials Letters, 2019, 236: 676−679.

[18] RAKHMONOV J U, VO N Q, CROTEAU J R, DORN J, DUNAND D C. Laser-melted Al−3.6Mn−2.0Fe−1.8Si−0.9Zr (wt%) alloy with outstanding creep resistance via formation of *α*-Al(FeMn)Si precipitates [J]. Additive Manufacturing, 2022, 60: 103285.

[19] ZHAO Cheng-zhang, REN Pei-rong, ZUO Zheng-xing, LI Dong-wei, LENG Guang, HUANG Wei-qing. The effect of thermal exposure on the microstructure and mechanical properties of cast Al−Si alloy for the cylinder head [J]. Materials Today Communications, 2023, 35: 105944.

[20] MA Ru-long, PENG Chao-qun, CAI Zhi-yong, WANG Ri-chu, ZHOU Zhao-hui, LI Xiao-geng, CAO Xuan-yang. Finite element analysis of temperature and stress fields during selective laser melting process of Al−Mg−Sc−Zr alloy [J]. Transactions of Nonferrous Metals Society of China, 2021, 31(10): 2922−2938.

[21] BISHT M S, GAUR V, SINGH I V. On mechanical properties of SLM Al−Si alloy: Role of heat treatment-induced evolution of silicon morphology [J]. Materials Science and Engineering: A, 2022, 858: 144157.

[22] DENG Jun-wang, CHEN Chao, LIU Xiao-chun, LI Yun-ping, ZHOU Ke-chao, GUO Sheng-min. A high-strength heat-resistant Al−5.7Ni eutectic alloy with spherical Al_3Ni nano-particles by selective laser melting [J]. Scripta Materialia, 2021, 203: 114034.

[23] BASAK C B, MEDURI A, HARI BABU N H. Influence of Ni in high Fe containing recyclable Al−Si cast alloys [J]. Materials & Design, 2019, 182: 108017.

[24] CHEN Biao, MOON S K, YAO Xi-ling, BI Gui-jun, SHEN Jiang-hua, UMEDA J, KONDOH K. Strength and strain hardening of a selective laser melted AlSi10Mg alloy [J]. Scripta Materialia, 2017, 141: 45−49.

[25] WANG Pei, ECKERT J, PRASHANTH K G, WU Ming-wei, KABAN I, XI Li-xia, SCUDINO S. A review of particulate-reinforced aluminum matrix composites fabricated by selective laser melting [J]. Transactions of Nonferrous Metals Society of China, 2020, 30(8): 2001−2034.

[26] CAI Qing, LORDAN E, WANG Shi-hao, LIU Guang-yu, MENDIS C L, CHANG I T H, JI Shou-xun. Die-cast multicomponent near-eutectic and hypoeutectic Al−Si−Ni−Fe−Mn alloys: Microstructures and mechanical properties [J]. Materials Science and Engineering: A, 2023, 872: 144977.

[27] DING Li-peng, ZHANG Xue-mei, LU Chang, WANG Cheng-lin, WENG Yao-yao, DONG Qi-peng, XU Shao-qiang, CAO Ling-fei, JIA Zhi-hong. Influence of the combined additions Mn, Cr or Ni on the formation of dispersoids and mechanical properties of Al−Mg−Si−Cu alloys [J]. Materials Science and Engineering: A, 2024, 892: 145962.

[28] ZHANG Xiao-zu, WANG Dong-tao, LI Xin-zhong, ZHANG Hai-tao, NAGAUMI H. Understanding crystal structure and morphology evolution of Fe, Mn, Cr-containing phases in Al−Si cast alloy [J]. Intermetallics, 2021, 131: 107103.

[29] ZHAO Lv, SONG Lu-bin, MACIAS J G S, ZHU Ya-xin, HUANG Min-sheng, SIMAR A, LI Zhen-huan. Review on the correlation between microstructure and mechanical performance for laser powder bed fusion AlSi10Mg [J]. Additive Manufacturing, 2022, 56: 102914.

[30] RINCÓN E, LÓPEZ H F, CISNEROS M M, MANCHA H, CISNEROS M A. Effect of temperature on the tensile properties of an as-cast aluminum alloy A319 [J]. Materials Science and Engineering: A, 2007, 452/453: 682−687.

[31] SHAHA S K, CZERWINSKI F, KASPRZAK W, FRIEDMAN J, CHEN D L. Ageing characteristics and high-temperature tensile properties of Al−Si−Cu−Mg alloys with micro-additions of Cr, Ti, V and Zr [J]. Materials Science and Engineering: A, 2016, 652: 353−364.

[32] WANG En-rui, HUI Xi-dong, CHEN Guang-liang. Eutectic Al−Si−Cu−Fe−Mn alloys with enhanced mechanical properties at room and elevated temperature [J]. Materials & Design, 2011, 32(8/9): 4333−4340.

[33] HAN Li-na, SUI Yu-dong, WANG Qu-dong, WANG Kui, JIANG Ye-hua. Effects of Nd on microstructure and mechanical properties of cast Al−Si−Cu−Ni−Mg piston alloys [J]. Journal of Alloys and Compounds, 2017, 695: 1566−1572.

[34] LIN Bo, FAN Tao, LI Hao-yu, ZHAO Yu-liang, ZHANG Wei-wen, LIU Kun. Microstructure and high temperature tensile properties of Al−Si−Cu−Mn−Fe alloys prepared by semi-solid thixoforming [J]. Transactions of Nonferrous Metals Society of China, 2021, 31(8): 2232−2249.

[35] SUWANPREECHA C, PANDEE P, PATAKHAM U, LIMMANEEVICHITR C. New generation of eutectic Al−Ni casting alloys for elevated temperature services [J]. Materials Science and Engineering: A, 2018, 709: 46−54.

[36] CHEN Jin-long, LIAO Heng-cheng, WU Yu-na, LI Hua-long. Contributions to high temperature strengthening from three types of heat-resistant phases formed during solidification, solution treatment and ageing treatment of Al−Cu−Mn−Ni alloys respectively [J]. Materials Science and Engineering: A, 2020, 772: 138819.

[37] LIN Bo, HE Xiang-xiang, XU Rui, ZHAO Yu-liang, LU Ye-mao, XIAO Hua-qiang. Evolution of iron-rich intermetallics and its effect on the mechanical properties of Al−Cu−Mn−Fe−Si alloys after thermal exposure and high-temperature tensile testing [J]. Journal of Materials Research and Technology, 2023, 23: 2527−2541.

[38] SU M N, YOUNG B. Material properties of normal and high strength aluminium alloys at elevated temperatures [J]. Thin-Walled Structures, 2019, 137: 463−471.

[39] RINCON E, LOPEZ H F, CISNEROS M M, MANCHA H. Temperature effects on the tensile properties of cast and heat treated aluminum alloy A319 [J]. Materials Science and Engineering: A, 2009, 519(1/2): 128−140.

[40] HOU Ruo-song, CHEN Jian-hao, REN Xue-peng, ZHAO Yang, DING Yu-feng, YU Zun-yue, REN Shu-bin, QU Xuan-hui. Effect of Ti microalloying and laser remelting on the microstructure and mechanical properties of laser powder bed fusion Al−12Si alloy [J]. Materials Science and Engineering: A, 2024, 901: 146548.

[41] ZHU Hao-wen, SUN Jia-wei, GUO You-jie, XU Xuan-xi, HUANG Yu-chuan, JIANG Zhi-da, WU Guo-hua, LI Jun-feng, LIU Wen-cai. Selective laser melting of a novel Al−Si−Fe−Mn−Ni alloy with superior mechanical properties at both room and elevated temperatures: Influence of processing parameters and heat treatment [J]. Materials Characterization, 2024, 214: 114098.

[42] YANG Zi-wei, CHEN Chao, LI Dan, WU Yi-you, GENG Zhao-wen, KONAKOV V, ZHOU Ke-chao. An additively manufactured heat-resistant Al−Ce−Sc−Zr alloy: Microstructure, mechanical properties and thermal stability [J]. Materials Science and Engineering: A, 2023, 872: 144965.

[43] PLOTKOWSKI A, SISCO K, BAHL S, SHYAM A, YANG Y, ALLARD L, NANDWANA P, ROSSY A M, DEHOFF R R. Microstructure and properties of a high temperature Al−Ce−Mn alloy produced by additive manufacturing [J]. Acta Materialia, 2020, 196: 595−608.

[44] BAHL S, PLOTKOWSKI A, SISCO K, LEONARD D N, ALLARD L F, MICHI R A, POPLAWSKY J D, DEHOFF R, SHYAM A. Elevated temperature ductility dip in an additively manufactured Al−Cu−Ce alloy [J]. Acta Materialia, 2021, 220: 117285.

[45] KIMURA T, NAKAMOTO T, OZAKI T, MIKI T. Microstructures and mechanical properties of aluminum−transition metal binary alloys (Al−Fe, Al−Mn, and Al−Cr) processed by laser powder bed fusion [J]. Journal of Alloys and Compounds, 2021, 872: 159680.

[46] ZHANG Jin-liang, SONG Bo, WEI Qing-song, BOURELL D, SHI Yu-sheng. A review of selective laser melting of aluminum alloys: Processing, microstructure, property and developing trends [J]. Journal of Materials Science & Technology, 2019, 35(2): 270−284.

[47] WANG Yue-ting, LI Rui-di, YUAN Tie-chui, ZOU Liang, WANG Mmin-bo, YANG Hai-ou. Microstructure and mechanical properties of Al−Fe−Sc−Zr alloy additively manufactured by selective laser melting [J]. Materials Characterization, 2021, 180: 111397.

[48] LI Xiao-peng, WANG Xiao-jun, SAUNDERS M, SUVOROVA A, ZHANG Lai-chang, LIU Yu-jing, FANG Mimg-hao, HUANG Zhao-hui, SERCOMBE T B. A selective laser melting and solution heat treatment refined Al−12Si alloy with a controllable ultrafine eutectic microstructure and 25% tensile ductility [J]. Acta Materialia, 2015, 95: 74−82.

[49] SU Xiang, LEI Yuan, CHEN Yang, QU Hong-jie, QI Zhi-xiang, ZHENG Gong, LIU Xu, XIANG Heng-gao, CHEN Guang. Precipitating thermally reinforcement phase in aluminum alloys for enhanced strength at 400 °C [J]. Journal of Materials Science & Technology, 2024, 172: 71−82.

[50] BUGELNIG K, SKET F, GERMANN H, STEFFENS T, KOOS R, WILDE F, BOLLER E, REQUENA G. Influence of 3D connectivity of rigid phases on damage evolution during tensile deformation of an AlSi12Cu4Ni2 piston alloy [J]. Materials Science and Engineering: A, 2018, 709: 193−202.

适于激光粉末床熔融成形的高强耐热 Al−Si−Fe 合金成分设计

郜文哲[1]，张 利[1,2]，李开洋[3]，杨晓辉[4]，张锦芳[1]，
王建宏[1]，徐 宏[1]，白培康[1]，曹远奎[5]，刘 彬[5]，李晓峰[1,5]

1. 中北大学 材料科学与工程学院，太原 030051；
2. 中北大学 特种金属材料与装备研究院，太原 030051；
3. 华北电力大学 能源与动力工程学院，北京 102206；
4. 海安太原理工大学 先进制造与智能装备产业研究院，海安 226600；
5. 中南大学 粉末冶金全国重点实验室，长沙 410083

摘 要：采用铸造和激光重熔相结合的方法，开发出一种适于激光粉末床熔融(PBF-LB)成形的高强耐热 Al−Si−Fe 合金。通过分析所添加合金元素的种类及含量对 Al−Si−Fe 合金显微组织和力学性能的影响，优选出一种 Al−11Si−2.5Fe−2Mn−1.2Ni−0.4Cr(质量分数，%)合金成分。随后，采用 PBF-LB 对所优选的合金开展成形验证，其密度达到 99.8%，表现出良好的成形性能。PBF-LB 成形 Al−Si−Fe 合金的室温抗拉强度达到(512.76±3.26) MPa，屈服强度为(337.79±2.36) MPa，伸长率为(2.98±0.07)%；材料室温力学性能的提高主要归因于细晶粒强化、固溶强化和析出强化的综合作用。所开发合金在 300 ℃的高温抗拉强度达到(222.47±6.41) MPa，屈服强度为(164.25±11.40) MPa，伸长率为(8.88±0.33)%，优于现有文献中合金的相应性能；高温力学性能的提高主要得益于由呈蜂窝状分布的 $Al_{17}(FeMnNiCr)_4Si_2$ 和 α-Al(FeMn)Si 耐热相组成的三维网络结构。

关键词：Al−Si−Fe 合金；激光粉末床熔融；合金成分优化；耐热相；强化机制

(Edited by Wei-ping CHEN)